The stellar velocity dispersion in nearby spirals: radial profiles and correlations

Monthly Notices
of the
ROYAL ASTRONOMICAL SOCIETY

MNRAS **489,** 3797–3809 (2019)
Advance Access publication 2019 August 26

doi:10.1093/mnras/stz2370

The stellar velocity dispersion in nearby spirals: radial profiles and correlations

Keoikantse Moses Mogotsi[1,2]★ and Alessandro B. Romeo[3]

[1] *South African Astronomical Observatory, P.O. Box 9, Observatory, 7935, Cape Town, South Africa*
[2] *Southern African Large Telescope Foundation, P.O. Box 9, Observatory, 7935, Cape Town, South Africa*
[3] *Department of Space, Earth and Environment, Chalmers University of Technology, SE-41296 Gothenburg, Sweden*

Accepted 2019 August 9. Received 2019 August 9; in original form 2018 April 26

ABSTRACT

The stellar velocity dispersion, σ, is a quantity of crucial importance for spiral galaxies, where it enters fundamental dynamical processes such as gravitational instability and disc heating. Here we analyse a sample of 34 nearby spirals from the Calar Alto Legacy Integral Field Area (CALIFA) spectroscopic survey, deproject the line-of-sight σ to σ_R, and present reliable radial profiles of σ_R as well as accurate measurements of $\langle\sigma_R\rangle$, the radial average of σ_R over one effective (half-light) radius. We show that there is a trend for σ_R to increase with decreasing R, that $\langle\sigma_R\rangle$ correlates with stellar mass ($M_\star$), and tested correlations with other galaxy properties. The most significant and strongest correlation is the one with $M_\star$: $\langle\sigma_R\rangle \propto M_\star^{0.5}$. This tight scaling relation is applicable to spiral galaxies of type Sa–Sd and stellar mass $M_\star \approx 10^{9.5}$–$10^{11.5}\,\mathrm{M}_\odot$. Simple models that relate σ_R to the stellar surface density and disc scale length roughly reproduce that scaling, but overestimate $\langle\sigma_R\rangle$ significantly.

Key words: instabilities – ISM: kinematics and dynamics – galaxies: ISM – galaxies: kinematics and dynamics – galaxies: star formation – galaxies: structure.

1 INTRODUCTION

The stellar velocity dispersion is an important parameter in stellar disc dynamics and has a wide range of applications. The various velocity dispersion components are used to study the distribution of stars near the solar neighbourhood (e.g. Dehnen 1998; Dehnen & Binney 1998; Tian et al. 2015) and how stars of different ages are distributed (e.g. Wielen 1977; Dehnen & Binney 1998; Binney, Dehnen & Bertelli 2000). This is used to make more detailed characterization of the structure and evolution of the Milky Way's stellar disc and its different components. These detailed local observations show the anisotropy between the radial, azimuthal, and vertical stellar velocity dispersion components such that $\sigma_R > \sigma_\phi > \sigma_z$. The ratios of these components (anisotropy parameters) are often thought of as the velocity ellipsoid (e.g. Schwarzschild 1907) and are crucial to quantifying the anisotropy and understanding its causes (e.g. Spitzer & Schwarzschild 1951; Jenkins & Binney 1990; Shapiro, Gerssen & van der Marel 2003; Gerssen et al. 2012; Pinna et al. 2018). In particular, σ_z/σ_R has a minimum of 0.3 due to the bending instability (Rodionov & Sotnikova 2013) and is used to constrain these 'disc heating' processes. σ_z is used to measure the mass-to-light-ratio of galactic discs (e.g. van der Kruit & Searle 1981; van der Kruit 1988; Bershady et al. 2010; Aniyan et al. 2018). In kinematic studies, σ_ϕ/σ_R is used to check the validity of the epicyclic approximation for stellar motions in the plane of a disc and σ_R is used to correct rotation curves for asymmetric drift (e.g. Binney & Tremaine 2008).

The stellar radial velocity dispersion, σ_R, is also one of the quantities that most radically affect the onset of gravitational instabilities in galaxy discs. It enters Toomre's (1964) stability criterion $Q \equiv \kappa\sigma_R/(3.36\,G\Sigma) \geq 1$ for infinitesimally thin stellar discs, as well as in more modern and advanced local stability analyses for multicomponent (e.g. Rafikov 2001; Leroy et al. 2008; Westfall et al. 2014) and realistically thick (e.g. Romeo & Falstad 2013) discs. Romeo & Mogotsi (2017) showed that stars, and not molecular or atomic gas, are the primary driver of disc instabilities in spiral galaxies, at least at the spatial resolution of current extragalactic surveys. This is true even for a powerful starburst and Seyfert galaxy like NGC 1068 (Romeo & Fathi 2016). Thus, σ_R is now recognized, more confidently than before, as a crucial quantity for disc instability.

It is difficult to obtain accurate and resolved measurements of stellar velocity dispersions for a large sample of galaxies and velocity dispersion components are difficult to disentangle from line-of-sight measurements (e.g. Gerssen, Kuijken & Merrifield 1997; Gerssen, Kuijken & Merrifield 2000; Shapiro, Gerssen & van der Marel 2003; Gerssen et al. 2012; Chemin 2018; Pinna et al. 2018). This is why disc stability analyses use model-based estimates of σ_R and make assumptions about the anisotropy parameters (e.g. Leroy et al. 2008; Romeo & Mogotsi 2017).

The advent of integral field surveys such as SAMI (Allen et al. 2015) and MaNGA (Bundy et al. 2015) is increasing the

★ E-mail: moses.mog@gmail.com

Table 1. Sample sizes of galaxies with relevant data.

Data	N
$\sigma_{\rm los}$, CSC[a], $M_\star$	74
$\sigma_{\rm los}$, CSC[a], $M_\star$, $M_{\rm mol}$, SFR, $l_\star$	34[b]
$\sigma_{\rm los}$, CSC[a], $M_\star$, $M_{\rm mol}$, SFR, $l_\star$, $\Sigma_\star$	24

Notes. Column 1: Data; Column 2: The number of Sa–Sd galaxies with relevant publicaly available data.
Sources of data: $\sigma_{\rm los}$ from F-B17; CSC[a] from K17; $M_\star$, $M_{\rm mol}$, SFR, and $l_\star$ from B17; and $\Sigma_\star$ from the CALIFA DR2 database.
[a]Circular-speed curve.
[b]The 34 galaxies include NGC2730, which has $l_\star$ calculated from $r_{\rm e}$.

number of galaxies with measured stellar kinematics. The Calar Alto Legacy Integral Field Area (CALIFA) survey (Sánchez et al. 2012) is a spatially resolved IFU spectroscopic survey of ∼600 nearby galaxies. The survey provides unprecedented detailed stellar kinematics for such a large and diverse sample of galaxies (e.g. Falcón-Barroso et al. 2017; Sánchez et al. 2017; Kalinova et al. 2017b). This enables a detailed study of stellar velocity dispersions out to one effective radius and to test stellar dispersion models. *Therefore, we aim to use this wealth of quality data to calculate* $\sigma_{\rm R}$. *We follow this by studying the radial behaviour of* $\sigma_{\rm R}$, *its relation to galaxy properties, and to test stellar velocity dispersion models for a sample of spiral galaxies across the Hubble sequence*.

We organize the paper as follows. The data are described in Section 2, the method and details about calculation of the σ_R and model-based dispersions are in Section 3. The results of the radial analysis, comparisons between observed and model-based dispersions, and relation to galaxy parameters are described in Section 4. These results are discussed in Section 5 and conclusions are in Section 6.

2 GALAXY SAMPLE AND DATA

This study is based on a sample of 34 nearby ($D < 122$ Mpc) spiral galaxies from the CALIFA survey (Sánchez et al. 2012). The sample consists of Sa to Sd galaxies for which resolved stellar velocity dispersions, accurate stellar circular-speed curves, molecular gas data, star formation rates, stellar masses, and stellar scale lengths are all publicly available. These are the data needed to calculate stellar radial velocity dispersions and test their correlations with galaxy properties, which we study in this paper and the following ones. The source of line-of-sight stellar velocity dispersions is the CALIFA high-resolution observations (using the V1200 grating to achieve R ∼1650 at a wavelength of ∼4500 Å) by Falcón-Barroso et al. (2017, hereafter F-B17), with a velocity resolution of $\sigma \sim 72\,{\rm km\,s^{-1}}$. We obtain molecular gas data from the EDGE-CALIFA survey, which is a resolved CO follow-up survey of 126 CALIFA galaxies with the CARMA interferometer by Bolatto et al. (2017, hereafter B17). It has yielded good-quality molecular gas data used in studies of the molecular gas properties of galaxies and in the role of gas and star formation in galaxy evolution. Finally, we obtain stellar circular-speed curves and dispersion anisotropy parameters from the study of Kalinova et al. (2017b, hereafter K17), who use the axisymmetric Jeans anisotropic multi-Gaussian expansion dynamical method (Cappellari 2008) to derive these values. Only 34 galaxies in the CALIFA sample have the requisite publicly available data at high enough quality for this analysis. The data requirements, sources of data, and samples of galaxies with the relevant publicly available data are summarized in Table 1.

We also select a subsample of galaxies for which stellar surface density data are available. This subsample consists of 24 galaxies and is crucial to compare the trends between σ_R and the modelled velocity dispersion $\sigma_{\rm mod}$ across a wide range of galaxy morphologies. B17 also use surface density maps to determine the exponential scale lengths of the galaxies that were used in this analysis. We obtain the stellar surface density $\Sigma_\star$ maps from Sánchez et al. (2016), who developed a pipeline called PIPE3D to determine dust-corrected $\Sigma_\star$ of CALIFA galaxies from the low-resolution CALIFA Data Release 2 (Sánchez et al. 2012; Walcher et al. 2014; García-Benito et al. 2015) V500 observations using stellar population fitting. It should be noted that the stellar masses for the entire sample were taken from B17; these values are the summation of stellar surface density maps determined using PIPE3D but they only publicly provide the stellar masses for these galaxies, hence still limiting our surface density subsample to 24 galaxies.

The maps and data used in this analysis are derived from Voronoi 2D binned (Cappellari & Copin 2003) data cubes. The galaxy sample covers a wide range of properties such as Hubble types ranging between Sa and Sd, stellar masses ranging between 9.84 and 11.27 $\log(M_\star/{\rm M}_\odot)$, and star formation rates between 0.7 and 15.1 ${\rm M}_\odot\,{\rm yr}^{-1}$. The global properties of the galaxy sample are shown in Table 2. We use the galaxy properties, dispersion maps, stellar surface density maps, circular-speed curves, and dispersion anisotropy values for our analysis.

3 METHOD

We derive the radial velocity dispersion σ_R maps from $\sigma_{\rm los}$ maps using the thin-disc approach (see e.g. Binney & Merrifield 1998). First, the line-of-sight velocity dispersion is expressed in terms of the radial σ_R, tangential σ_ϕ, and vertical σ_z dispersion components by the general formula:

$$\sigma_{\rm los}^2 = \left(\sigma_R^2 \sin^2\phi + \sigma_\phi^2 \cos^2\phi\right) \sin^2 i + \sigma_z^2 \cos^2 i, \quad (1)$$

which requires the inclination angle of the galaxy i and the position angle of the galaxy ϕ (e.g. Binney & Merrifield 1998). Romeo & Fathi (2016) define two parameters (based on the axial ratios of the dispersion anisotropy components): $A = \sigma_\phi/\sigma_R$ and $B = \sigma_z/\sigma_R$ in order to rewrite the above equation in the form

$$\sigma_R = \sigma_{\rm los}\left[\left(\sin^2\phi + A^2\cos^2\phi\right)\sin^2 i + B^2\cos^2 i\right]^{-1/2}. \quad (2)$$

Following the epicyclic approximation of an axisymmetric disc with approximately circular orbits $A \approx \kappa/2\Omega$ (e.g. Binney & Tremaine 2008), where Ω is the angular frequency and κ the epicyclic frequency. Each of these parameters can be determined from circular velocity $v_{\rm c}(R)$ as follows: $\Omega = v_{\rm c}(R)/R$ and $\kappa = \sqrt{R\,{\rm d}\Omega^2/{\rm d}R + 4\Omega^2}$.

We use K17 circular-speed curves to calculate κ and Ω, from which we calculate A, and use their dispersion anisotropy parameter $\beta_z = 1 - \sigma_z^2/\sigma_R^2$. We calculate B using $B = \sqrt{1-\beta_z^2}$. Therefore, we have the necessary parameters to calculate σ_R from $\sigma_{\rm los}$ using equation (1), thus we use maps of A, B, ϕ, and $\sigma_{\rm los}$ to calculate σ_R and produce maps of it for each galaxy. An example of a σ_R map is showed in Fig. 1.

We use $\sigma_{\rm los}$ maps to mask out unreliable σ_R values by imposing $40\,{\rm km\,s^{-1}}$ as a lower limit on our $\sigma_{\rm los}$, because F-B17 compared their $\sigma_{\rm los}$ values with higher resolution $\sigma_{\rm los}$ observations and found that the CALIFA $\sigma_{\rm los}$ values and their associated uncertainties are highly unreliable for $\sigma < 40\,{\rm km\,s^{-1}}$. We further apply a cut-off to exclude data with relative uncertainties greater than 20 per cent. This value is based on the median relative uncertainty of data with

Table 2. Galaxy properties.

Name	Type	σ_z/σ_R	12+log(O/H)	log $M_\star$ ($M_\odot$)	log $M_{\rm mol}$ ($M_\odot$)	log SFR ($M_\odot$ yr^{-1})	$l_\star$ (kpc)	$l_{\rm mol}$ (kpc)	$l_{\rm SFR}$ (kpc)
(1)	(2)	(3)	(4)	(5)	(6)	(7)	(8)	(9)	(10)
IC 0480	Sbc	0.80 ± 0.01	8.49 ± 0.05	10.27 ± 0.13	9.55 ± 0.02	0.11 ± 0.10	3.08 ± 0.32	2.23 ± 0.43	2.58 ± 0.41
IC 0944	Sa	0.75 ± 0.01	8.52 ± 0.06	11.26 ± 0.10	10.00 ± 0.02	0.41 ± 0.15	5.06 ± 0.15	5.16 ± 0.90	8.70 ± 0.79
IC 2247	Sbc	0.72 ± 0.01	8.51 ± 0.04	10.44 ± 0.11	9.47 ± 0.02	0.23 ± 0.15	2.62 ± 0.13	2.91 ± 0.79	2.79 ± 0.46
IC 2487	Sb	0.63 ± 0.01	8.52 ± 0.05	10.59 ± 0.12	9.34 ± 0.04	0.17 ± 0.08	3.83 ± 0.09	3.82 ± 1.03	5.36 ± 0.54
NGC 2253	Sc	0.43 ± 0.01	8.59 ± 0.04	10.81 ± 0.11	9.62 ± 0.02	0.50 ± 0.06	2.48 ± 0.18	2.83 ± 0.85	1.82 ± 0.52
NGC 2347	Sbc	0.63 ± 0.01	8.57 ± 0.04	11.04 ± 0.10	9.56 ± 0.02	0.54 ± 0.07	2.16 ± 0.06	2.45 ± 0.68	1.37 ± 0.35
NGC 2410	Sb	0.89 ± 0.03	8.52 ± 0.05	11.03 ± 0.10	9.66 ± 0.03	0.55 ± 0.11	3.22 ± 0.13	4.09 ± 1.29	3.42 ± 0.19
NGC 2730	Sd	0.79 ± 0.02	8.45 ± 0.04	10.13 ± 0.09	9.00 ± 0.06	0.23 ± 0.06	(3.80)[a]	–	11.61 ± 4.11
NGC 4644	Sb	1.30 ± 0.04	8.59 ± 0.04	10.68 ± 0.11	9.20 ± 0.05	0.09 ± 0.09	2.64 ± 0.18	7.18 ± 3.37	5.26 ± 0.80
NGC 4711	SBb	0.93 ± 0.05	8.60 ± 0.04	10.58 ± 0.09	9.18 ± 0.05	0.08 ± 0.07	3.01 ± 0.11	5.59 ± 5.41	3.13 ± 0.68
NGC 5056	Sc	1.09 ± 0.06	8.49 ± 0.03	10.85 ± 0.09	9.45 ± 0.04	0.57 ± 0.06	2.96 ± 0.08	4.37 ± 1.60	4.68 ± 0.59
NGC 5614	Sab	1.00 ± 0.81	8.55 ± 0.06	11.22 ± 0.09	9.84 ± 0.01	0.20 ± 0.11	2.31 ± 0.21	1.04 ± 0.50	3.04 ± 1.04
NGC 5908	Sb	1.01 ± 0.12	8.54 ± 0.05	10.95 ± 0.10	9.94 ± 0.01	0.36 ± 0.08	3.21 ± 0.07	3.25 ± 0.48	2.32 ± 0.24
NGC 5980	Sbc	0.77 ± 0.01	8.58 ± 0.03	10.81 ± 0.10	9.70 ± 0.02	0.71 ± 0.06	2.37 ± 0.05	2.60 ± 0.60	1.87 ± 0.30
NGC 6060	SABc	0.82 ± 0.03	8.50 ± 0.08	10.99 ± 0.09	9.68 ± 0.03	0.62 ± 0.14	3.90 ± 0.21	6.09 ± 1.77	5.31 ± 1.07
NGC 6168	Sd	0.67 ± 0.01	8.40 ± 0.03	9.94 ± 0.11	8.65 ± 0.06	−0.07 ± 0.06	2.42 ± 0.40	–	1.68 ± 0.53
NGC 6186	Sa	0.88 ± 0.04	8.59 ± 0.04	10.62 ± 0.09	9.46 ± 0.02	0.30 ± 0.06	2.43 ± 0.11	2.25 ± 0.45	1.66 ± 0.40
NGC 6314	Sa	0.54 ± 0.01	8.49 ± 0.06	11.21 ± 0.09	9.57 ± 0.03	0.00 ± 0.28	3.77 ± 0.21	2.25 ± 0.08	0.97 ± 0.18
NGC 6478	Sc	0.62 ± 0.01	8.56 ± 0.04	11.27 ± 0.10	10.14 ± 0.02	1.00 ± 0.07	6.23 ± 0.27	6.60 ± 1.13	15.99 ± 4.00
NGC 7738	Sb	0.70 ± 0.03	8.56 ± 0.06	11.21 ± 0.11	9.99 ± 0.01	1.18 ± 0.09	2.30 ± 0.24	1.68 ± 0.54	1.14 ± 0.20
UGC 00809	Sc	0.68 ± 0.01	8.41 ± 0.03	10.00 ± 0.13	8.92 ± 0.07	−0.14 ± 0.08	3.84 ± 0.16	6.14 ± 3.15	2.99 ± 0.36
UGC 03253	Sb	1.21 ± 0.03	8.51 ± 0.07	10.63 ± 0.11	8.88 ± 0.06	0.23 ± 0.11	2.42 ± 0.09	5.14 ± 1.58	3.16 ± 1.03
UGC 03539	Sbc	1.25 ± 0.07	8.39 ± 0.07	9.84 ± 0.13	9.11 ± 0.03	−0.17 ± 0.09	1.46 ± 0.02	1.58 ± 1.03	1.62 ± 0.15
UGC 04029	Sbc	0.78 ± 0.02	8.48 ± 0.08	10.38 ± 0.10	9.37 ± 0.03	0.18 ± 0.09	3.38 ± 0.16	4.03 ± 0.97	4.33 ± 0.34
UGC 04132	Sbc	0.99 ± 0.33	8.54 ± 0.04	10.94 ± 0.12	10.02 ± 0.01	0.96 ± 0.07	3.63 ± 0.16	3.13 ± 0.62	4.42 ± 0.49
UGC 05108	SBab	1.16 ± 0.03	8.50 ± 0.06	11.11 ± 0.11	9.75 ± 0.04	0.66 ± 0.12	3.79 ± 0.10	2.75 ± 0.80	2.72 ± 0.28
UGC 05598	Sbc	0.54 ± 0.01	8.45 ± 0.05	10.40 ± 0.12	9.17 ± 0.06	0.15 ± 0.09	3.09 ± 0.21	2.68 ± 0.72	4.59 ± 0.51
UGC 09542	Sc	0.46 ± 0.01	8.49 ± 0.05	10.53 ± 0.13	9.31 ± 0.05	0.27 ± 0.09	3.45 ± 0.10	5.44 ± 2.24	5.96 ± 1.05
UGC 09873	Sc	0.76 ± 0.02	8.46 ± 0.05	10.21 ± 0.10	9.08 ± 0.07	0.10 ± 0.09	3.69 ± 0.14	2.86 ± 0.94	2.97 ± 0.27
UGC 09892	Sb	1.04 ± 0.30	8.48 ± 0.05	10.48 ± 0.10	9.17 ± 0.05	−0.03 ± 0.08	2.90 ± 0.12	5.72 ± 2.05	4.78 ± 0.61
UGC 10123	Sab	0.72 ± 0.01	8.54 ± 0.03	10.30 ± 0.10	9.48 ± 0.02	0.21 ± 0.07	1.62 ± 0.11	2.23 ± 0.59	2.19 ± 0.20
UGC 10205	Sa	0.97 ± 0.07	8.49 ± 0.04	11.08 ± 0.10	9.60 ± 0.04	0.38 ± 0.20	3.12 ± 0.09	2.94 ± 0.84	2.01 ± 0.06
UGC 10384	Sab	0.70 ± 0.01	8.50 ± 0.05	10.33 ± 0.14	9.10 ± 0.02	0.65 ± 0.06	1.53 ± 0.10	1.77 ± 0.29	1.84 ± 0.16
UGC 10710	Sb	0.66 ± 0.01	8.52 ± 0.05	10.92 ± 0.09	9.88 ± 0.04	0.50 ± 0.10	5.15 ± 0.42	4.39 ± 0.96	4.62 ± 0.55

Notes. Column 1: galaxy name; Column 2: Hubble type; Column 3: the ratio of vertical to radial velocity dispersion calculated from β_z derived by K17; Column 4: metallicity; Column 5: stellar mass; Column 6: molecular gas mass; Column 7: star formation rate; Column 8: stellar scale length; Column 9: molecular gas scale length; Column 10: star formation scale length. Columns 2 and 4–10 are from B17.
[a]The scale length for NGC 2730 is estimated using $l_* = R_e/1.68$.

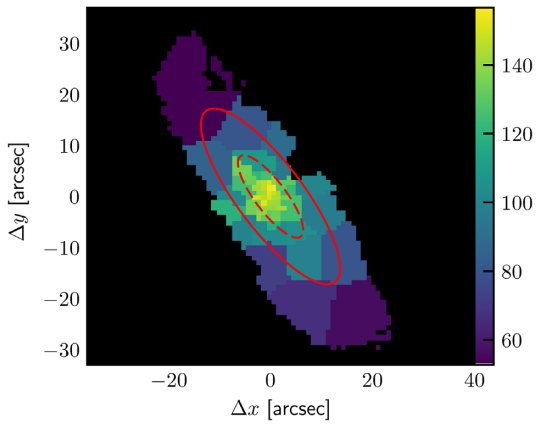

Figure 1. A map of the stellar radial velocity dispersion σ_R in NGC 2410; the colour bar represents σ_R values in units of km s^{-1}. The red solid line represents one effective radius R_e and the red dashed line represents one stellar scale length l_s.

$\sigma \sim 40$ km s^{-1} being 20 per cent (F-B17). After we apply these, we are left with reliable σ_R maps for each galaxy.

We derive the radial profiles of σ_R by dividing σ_R maps into tilted rings that are circular in the plane of the galaxy. Each tilted ring is defined by a kinematically derived (where possible) inclination and position angle taken from B17, and the galaxy centre is defined as the photometric centre adopted by F-B17 in their $\sigma_{\rm los}$ maps (Husemann et al. 2013). Fig. 1 shows an example of azimuthal rings defined by the effective radius and stellar scale length. Then we calculate the median and its associated uncertainty for each radial bin of width 0.2 R_e. Only annuli that contain more than two data points are used for the $\sigma_R(R)$ calculations. In such data, some individual rings contain few data points and some have a large fraction of outliers, therefore we use the median and its associated uncertainty for robust statistical measures (e.g. Rousseeuw 1991; Müller 2000; Romeo, Horellou & Bergh 2004; Huber & Ronchetti 2009; Feigelson & Babu 2012). In our study, we calculate the uncertainty of the median by using the median absolute deviation (MAD):

$$\Delta X_{\rm med} = 1.858 \times {\rm MAD}/\sqrt{\rm N}, \quad (3)$$

$$\mathrm{MAD} = \mathrm{median}\{|\mathrm{X_i} - \mathrm{X_{med}}|\}, \quad (4)$$

where X_i are individual measurements, $X_{\rm med}$ is their median value, and N is the number of pixels (Voronoi bin centres) in each ring where there are detections. These equations are robust counterparts of the mean uncertainty formula that uses the standard deviation (SD): $\Delta X_{\rm mean} = SD/\sqrt{N}$ (Müller 2000). We use these medians and associated uncertainties to determine the final radial profiles for σ_R and A. The uncertainties do not take into account the covariance between bins.

The third step of the data analysis is to compare σ_R with modelled radial dispersions $\sigma_{\rm mod}$. We use the common approach used by (Leroy et al. 2008, hereafter L08) to determine $\sigma_{\rm mod}$ (see Appendix B.3 of L08):

$$\sigma_{\rm mod} = \frac{1}{0.6}\sqrt{\frac{2\pi G l_\star}{7.3}}\,\Sigma_\star^{0.5}, \quad (5)$$

where $l_\star$ is the stellar exponential scale length and $\Sigma_\star$ is the stellar surface density.

This model assumes that the exponential scale height of a galaxy does not vary with radius, the flattening ratio between the scale height and scale length is 7.3 (Kregel, van der Kruit & de Grijs 2002), that discs are in hydrostatic equilibrium and that they are isothermal in the z-direction (e.g. van der Kruit & Searle 1981; van der Kruit 1988), and that σ_z/σ_R =0.6 (e.g. Shapiro et al. 2003). We investigate the effects of the flattening ratio and σ_z/σ_R assumptions on our analysis in Section 5.2. For each galaxy in our subsample, we take the $\Sigma_\star$ map and $l_\star$ values (from B17) and use equation (5) to derive a map of $\sigma_{\rm mod}$. Then we divide the $\sigma_{\rm mod}$ map into tilted rings that are circular in the plane of the galaxy. And we determine the radial profile by calculating the median and its associated uncertainty for each radial bin of width 0.2 $R_{\rm e}$. The outputs of this procedure are maps and radial profiles of $\sigma_{\rm mod}$ for each galaxy in our subsample.

4 RESULTS

4.1 Radial profiles

In Fig. 2, we show the σ_R of each Voronoi bin and as a function of galactocentric radius [$\sigma_R(R)$] for each galaxy in our sample. There are large variations in the radial behaviour of σ_R between galaxies, but the general trend is of decreasing σ_R with increasing R.

Comparisons between σ_R and $\sigma_{\rm mod}$ are displayed in Fig. 2. The radial behaviour of $\sigma_{\rm mod}$ is dominated by the typically exponential smooth decrease of $\Sigma_\star$ and in the figure we see a far more pronounced decrease of $\sigma_{\rm mod}$ with increasing R than for σ_R. Fig. 2 shows that $\sigma_{\rm mod}$ overestimates σ_R at low R, and in general at $R = l_\star$ we find that $\sigma_R < \sigma_{\rm mod}$. The data and shallower decline result in a switchover at larger R where $\sigma_R \geq \sigma_{\rm mod}$. However, due to the sparseness of σ_R data at large R, we cannot conclude that this is the general behaviour.

Fig. 3 shows the radial behaviour of A and B parameters calculated from kinematic parameters derived by K17. The parameter B is constant due to the assumption of a constant β_z by K17 and A typically decreases with increasing R from a maximum ∼1. There is a large variation in B between galaxies, ranging between 0.4 and 1.3, which is larger than found in previous studies and typically used in models (Shapiro et al. 2003; L08; Romeo & Fathi 2015, 2016; Pinna et al. 2018).

We now study the relationship between $\sigma_R(R)$ and galaxy properties. The data do not extend far out enough to determine whether the radial behaviour of σ_R correlates with any of the properties. In Fig. 4, we plot σ_R as a function of galactocentric radius and $M_\star$. It should be noted that measurements of $M_\star$ are limited to within the 74 arcsec × 64 arcsec field of view of the CALIFA observations, and González Delgado et al. (2014) showed that on average this can underestimate the total $M_\star$ by 8 per cent. There are large σ_R variations between and within galaxies as in Fig. 2. However, from the figure we see that galaxies with higher $M_\star$ tend to have larger σ_R. When we compare the radial behaviour of σ_R and other properties, we see no correlations; however, the relationships between different parameters and σ_R are discussed in more detail in the following section.

4.2 Correlations

We want to quantify the relationships between σ_R and different parameters over a physically significant region of the galaxy and hence calculate the radial average of $\sigma_R(R)$ over one effective (half-light) radius, robustly estimated via the median $\langle\sigma_R\rangle$ and its associated uncertainty for each galaxy. These are derived using the same method as $\sigma_R(R)$ but with a ring width equal to 1 $R_{\rm e}$. We do not apply any corrections for galaxies whose data do not extend to 1 $R_{\rm e}$. The $\langle\sigma_R\rangle$ for each galaxy are plotted against various properties in Fig. 5. The Pearson's and Spearman's correlation coefficients ($r_{\rm P}$ and $r_{\rm S}$, respectively), their corresponding p-values (which indicate the probability of a null hypothesis), and best-fitting linear parameters of each $\langle\sigma_R\rangle$–parameter plot are shown in Table 3. Linear fits were parametrized as follows: $\log\langle\sigma_R\rangle = a\log X + b$ for fits performed using the robust median method and $\log\langle\sigma_R\rangle = c\log X + d$ for fits performed using the least-squares orthogonal distance regression (ODR) method (see e.g. Press et al. 1992). The latter method takes into account uncertainties of both variables whereas the former does not take into account any uncertainties but is a more robust fitting method. The best-fitting lines and parameters are only shown in Fig. 5 and Table 3; for cases where there is a strong and significant correlation between variables, we define this case as $|r| > 0.5$ and $p < 0.05$. The relative strengths and significances of correlations are consistent whether the Pearson's or Spearman's correlation coefficients are used.

In Fig. 5, we see that $\langle\sigma_R\rangle$ is correlated with $M_\star$, $M_{\rm mol}$, and SFR, respectively. This is confirmed by the correlation coefficients shown in Table 4, which range from 0.42 (SFR) to 0.86 ($M_\star$). Among the galaxy properties, $M_\star$ has the strongest and most significant correlation with $\langle\sigma_R\rangle$; the correlation between them has $r_{\rm S} = 0.86$ and $p_{\rm S} = 1.0 \times 10^{-10}$. The best-fitting linear relationship is $\log\langle\sigma_R\rangle = (0.45 \pm 0.05)\log M_\star + (-2.78 \pm 0.51)$ with a root mean squared (rms) scatter of 0.10 dex (26 per cent); therefore $\langle\sigma_R\rangle \propto M_\star^{0.45}$. $M_{\rm mol}$ has the next strongest and significant correlation ($r_{\rm S} = 0.77$ and $p_{\rm S} = 1.0 \times 10^{-7}$) followed by SFR ($r_{\rm S} = 0.60$ and $p_{\rm S} = 1.8 \times 10^{-4}$). And their best-fitting relations have rms scatter values of 0.12 and 0.18 dex, respectively. The power-law indices of the $M_\star$, $M_{\rm mol}$, and SFR relations are close to 0.5 when uncertainties are taken into account; when no uncertainties are taken into account, the indices are lower and range between 0.29 and 0.32.

We also see weak $\langle\sigma_R\rangle$ correlations with Hubble type ($r_{\rm S} = -0.51$) and metallicity ($r_{\rm S} = 0.44$): both have lower significance than the aforementioned properties, and their p-values are less than 0.05. The other parameters (σ_z/σ_R, $l_\star$, $l_{\rm mol}$, $l_{\rm SFR}$) are not correlated with $\langle\sigma_R\rangle$, and their p-values are larger than 0.05.

Finally, we test the $\sigma_{\rm mod}$ model by determining the radial average of $\sigma_{\rm mod}$ (R) over 1 $R_{\rm e}$, robustly estimated via the median and

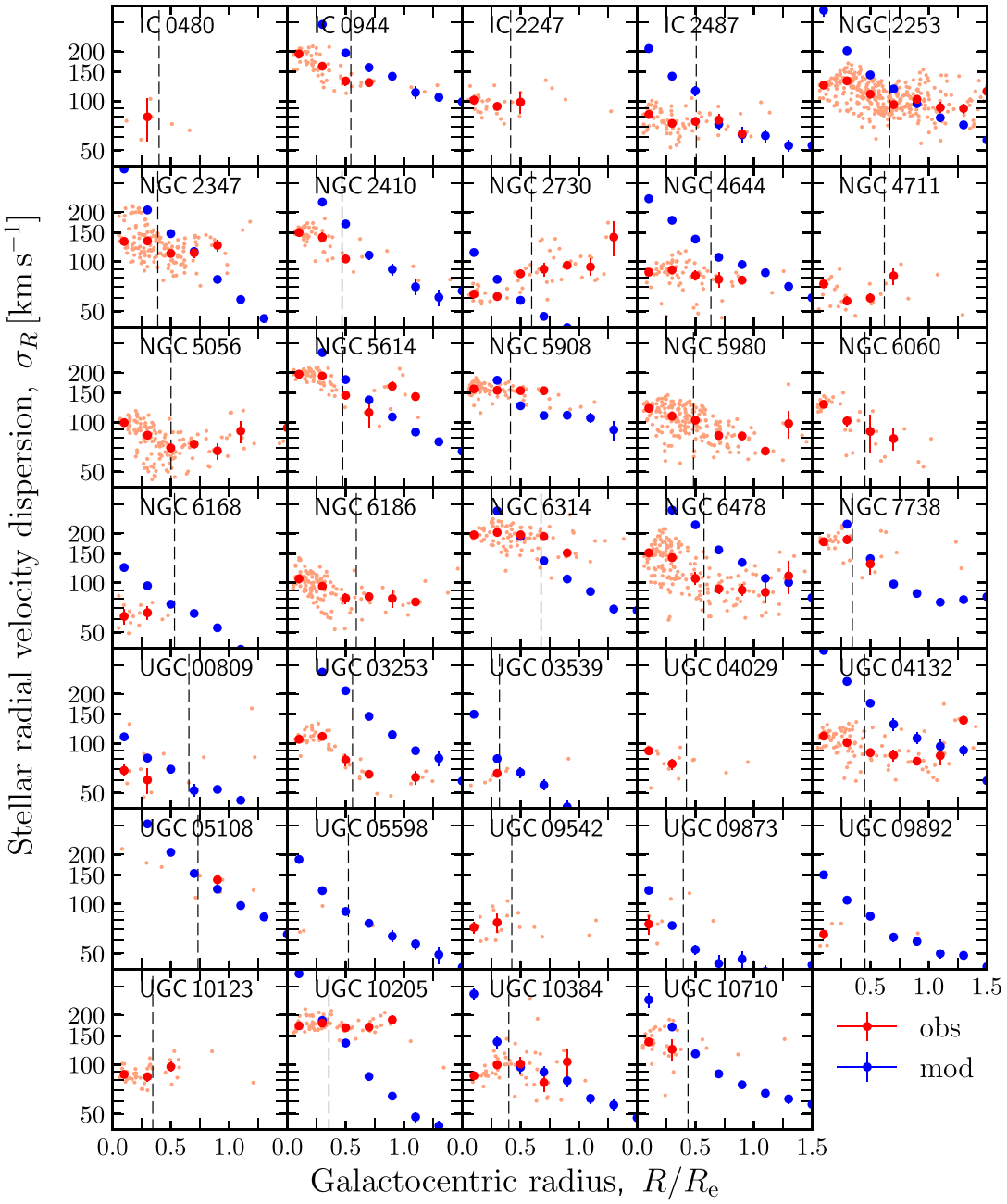

Figure 2. Stellar radial velocity dispersion σ_R as a function of galactocentric radius. The light red data points show individual σ_R measurements based on line-of-sight velocity dispersion measurements; the dark red data points are the medians and associated uncertainties for σ_R data in 0.2 R_e bins. The blue points are the medians and associated uncertainties of model-based velocity dispersions in 0.2 R_e bins. The vertical dashed lines indicate the stellar scale lengths.

comparing it with the observation-based $\langle \sigma_R \rangle$ in Fig. 6. We plot them against the velocity scale: $\sqrt{GM_\star/l_\star}$ determined from the global properties: $M_\star$ and $l_\star$. This was done for the 24/34 galaxies in our sample that have $\Sigma_\star$ maps available. Fig. 6 is consistent with the findings in Fig. 2 where we find that $\sigma_{\rm mod} > \sigma_R$ in the inner regions, and the difference between them tends to decrease as R increases. The data used in Fig. 6 are shown in Table 4. We see in Fig. 6 and Table 4 that $\langle \sigma_{\rm mod} \rangle > \langle \sigma_R \rangle$ for most galaxies. Fig. 6 has a separatrix line of $\langle \sigma_R \rangle = 0.4\sqrt{GM_\star/l_\star}$, derived by taking the radial average of equation (5) over R_e, which is where we expect the L08 $\sigma_{\rm mod}$ values to lie. $\langle \sigma_R \rangle$ values lie on or below this line and $\langle \sigma_{\rm mod} \rangle$ data tend to lie on or above this relation. Therefore, $\langle \sigma_{\rm mod} \rangle$ does not accurately model $\langle \sigma_R \rangle$.

The expected relation between σ_R and $\sqrt{GM_\star/l_\star}$ requires that (1) σ_R follow an exponential decline with radius and (2) that the spatial bin size of data points be equal. However, Fig. 2 shows that $\sigma_R(R)$ has a wide range of shapes even though it tends to decline with radius. Therefore, it is not always declining exponentially and due to the nature of our data the second condition of equal spatial bin sizes is not satisfied either. These are the likely reasons for $\langle \sigma_{\rm mod} \rangle$ not following a slope of 0.4.

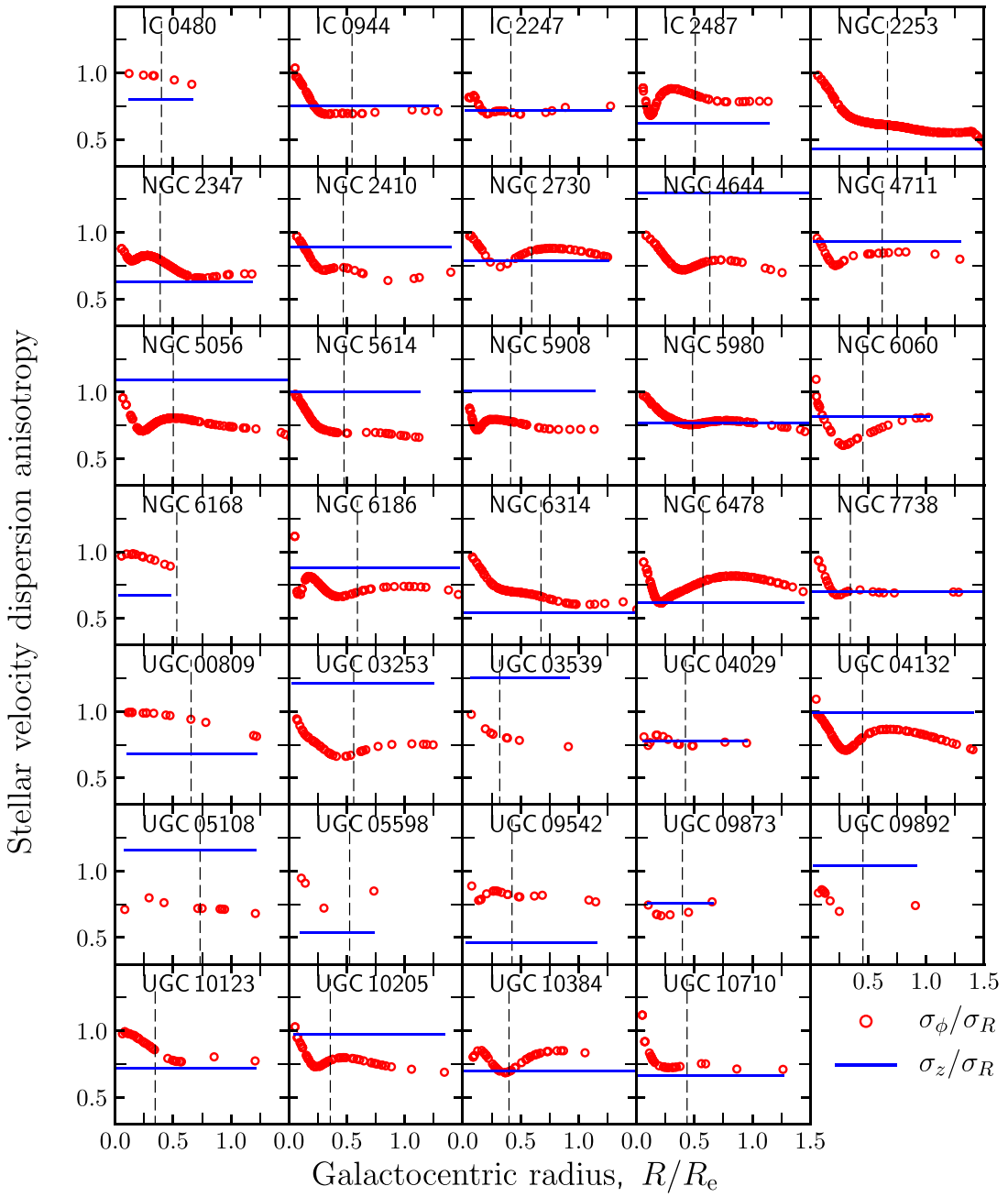

Figure 3. Stellar velocity dispersion anisotropy parameters as a function of galactocentric radius. The red circles are $A = \sigma_\phi/\sigma_R$ calculated at the galactocentric radius of each $\sigma_{\rm los}$ data point, and the blue lines show the constant $B = \sigma_z/\sigma_R$ calculated from β_z values derived by K17. The vertical dashed lines indicate the stellar scale lengths.

The fact that $\langle\,\sigma_{\rm mod}\,\rangle$ overestimates $\langle\,\sigma_R\,\rangle$ significantly in the inner stellar disc becomes even clearer if we consider the radial average of $\sigma_R(R)$ over one exponential scale length $l_\star$ ($R_e \sim 1.68 l_\star$) in Fig. 7. We see that the data are further away from the expected relation. The plot shows that $\langle\,\sigma_{\rm mod}\,\rangle$ overestimates the observationally based $\langle\,\sigma_R\,\rangle$ within $l_\star$, the differences are larger than in Fig. 6 and are greater than 50 km s^{-1} in the most extreme cases. This comparison confirms that the difference between $\langle\,\sigma_R\,\rangle$ and $\langle\,\sigma_{\rm mod}\,\rangle$ is largest at small radii.

5 DISCUSSION

5.1 Uncertainties in σ_R

Sources of uncertainty arise from the calculation of the anisotropy parameters and σ_R; these quantities are difficult to determine and require many assumptions (e.g. Hessman 2017; K17). Recent work has improved our ability to determine these parameters (e.g. Cappellari 2008; Bershady et al. 2010; Gerssen et al. 2012; Kalinova et al. 2017a; Marchuk & Sotnikova 2017; Chemin 2018; Pinna

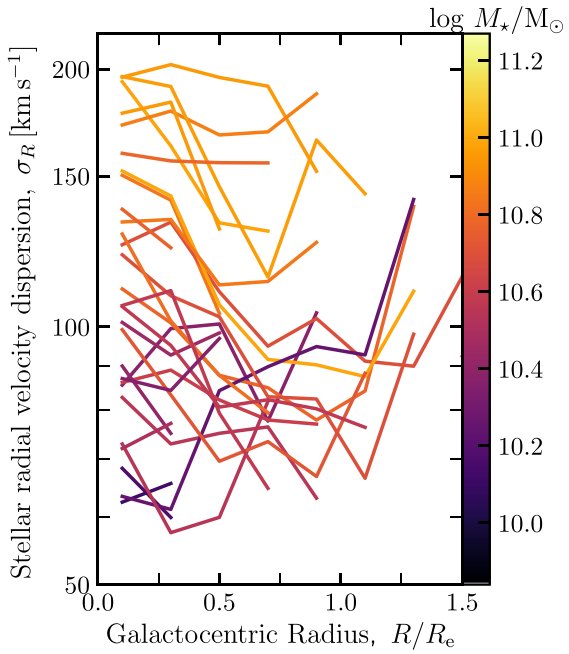

Figure 4. The stellar radial velocity dispersion as a function of galactocentric radius $\sigma_R(R)$ for each galaxy. Galaxies are colour coded according to $M_\star$. The $\sigma_R(R)$ values plotted are the medians of σ_R in 0.2 R_e bins.

et al. 2018). The σ_z/σ_R and σ_ϕ/σ_R values we use in this analysis are calculated from parameters derived by K17, who use modern sophisticated modelling to derive them from observations (see Cappellari 2008).

The σ_R values we use are derived from F-B17's CALIFA σ_los observations. The data are of high quality but are limited by the spatial resolution, sensitivity, and velocity resolution relative to typical σ_los of the survey, introducing uncertainties to our analysis. More galaxies and better radial data will improve our characterization of the radial behaviour and help to determine whether the radial trends are a function of other properties. We apply a dispersion cut-off and 20 per cent error cut-off to ensure that we use reliable and accurate data. The dispersion cut-off resulted in many low-σ_R data being excluded from our analysis. The loss of low-quality data points has the largest effect on our analysis at large radii, where there are few high-quality data suitable for our analysis. Despite these uncertainties, we can still conclude that σ_mod values overestimate σ_R at small R (particularly within $l_\star$) and the difference between σ_mod and σ_R decreases with increasing R for $R < R_\mathrm{e}$.

Inclination has an effect on the observed velocity dispersion because of line-of-sight projection effects and dust extinction. For highly inclined galaxies, individual fibres cover a wide range of galactocentric radii and galaxy kinematics, therefore each observed spectrum consists of a superposition of a large number of regions with different kinematics. Variation of the anisotropic stellar velocity ellipsoid complicates the extraction of stellar kinematics parameters further due to the combination of line-of-sight projected velocities and velocity dispersions in the projected spectra. Kregel & van der Kruit (2005) also showed how at high inclinations the line-of-sight projection effects cause increased asymmetry in the observed dispersion measurements, resulting in greater differences between the observed and true stellar velocity dispersions. The increased number of regions covering a wide range of azimuths in line-of-sight observations at high inclination means that equation (1) becomes a less accurate description of σ_los in such cases, and its use results in overestimation of σ_los and hence σ_R. Dust extinction along the line of sight can result in underestimation of the true R of σ_los measurements, which results in underestimation of σ_los at low radii. The interplay between stellar kinematics, inclination, and the dust extinction on σ_los is examined in more detail by Kregel & van der Kruit (2005). The inclination distribution of our 34 galaxy sample is shown in Fig. 8. The galaxies cover a wide range of inclinations between 30° and 80°, with a large number of galaxies with $70^\circ < i < 80^\circ$.

We also look at the relationship between σ_los and $M_\star$ and see that the best-fitting relationship is similar to the σ_R and $M_\star$ relationship but has slightly weaker correlation and slightly larger rms. The fitted relations are shown in Fig. 8; the best-fitting ODR relation is: $\log\langle\sigma_\mathrm{obs}\rangle = (0.46 \pm 0.05)\log M_\star + (-2.93 \pm 0.57)$ with an rms of 0.11. The figure also shows that galaxies across our inclination range lie on or close to the best-fitting relation. Some high-i and low-$M_\star$ galaxies have either underestimated $M_\star$ or overestimated σ_los with respect to the best-fitting relationship; both of these can occur due to line-of-sight effects. We also explore inclination effects as a function of R but find no correlation between $\sigma_R(R)$ profiles and i. Further investigation and modelling outside of the scope of this paper is required to better constrain the line-of-sight effects on σ_R and $M_\star$ measurements in the CALIFA sample, but in our analysis, we do not find evidence for i having a strong bias on σ_R and its relation with $M_\star$.

5.2 Comparison between σ_R and σ_mod

For the comparison with σ_mod, we assume $B = 0.6$; however, Fig. 3 shows that typical values of B for our sample are greater than 0.6. K17 also determined flattening ratios for their galaxies in their analysis. Such an analysis can improve σ_mod models but requires high-quality stellar kinematics data. We now study the effect of using parameters derived from modelling individual galaxies by determining σ_mod using B and flattening ratios determined by K17 and using a relation from Bershady et al. (2010). The B values are typically between a factor of 1 or 2 greater than the assumed values, and the fitted K17 on-sky flattening ratios are typically lower by up to a factor of ~2. Using these parameters results in small changes in σ_mod that vary between galaxies. However, when we combine the relation that Bershady et al. (2010) fitted between the flattening ratio q and $l_\star$: $\log(q) = 0.367\log(l_\star) + 0.708$ with K17's B values to determine σ_mod, we find that the σ_mod values overestimate σ_R in most cases but are smaller than those calculated using the parameters we used in the rest of the paper. This is seen in Fig. 9, where we plot σ_mod radially averaged (calculated using different parameters) over $l_\star$ versus the velocity scale. This shows that using better models for B and q can improve σ_R predictions, even in the inner regions of galaxies, but still overestimate σ_R. The overestimation is likely due to the departures from non-exponential decline with R of σ_R, as seen in the varying radial profiles of σ_R seen in Fig. 2.

The overestimation of σ_R has important consequences for stability analysis because lower σ_R results in lower disc stability. Romeo & Mogotsi (2017) studied the multicomponent disc stability, determining the σ_R using the L08 model, and found that inner discs are marginally unstable against non-axisymmetric perturbations and gas dissipation and that the stars drive disc instabilities in the inner regions of galaxies. Our results indicate that σ_R and hence the stability due to stars are overestimated by that model and therefore stars have an even greater effect on disc instabilities than Romeo & Mogotsi (2017) found. The dominance of the stellar disc is

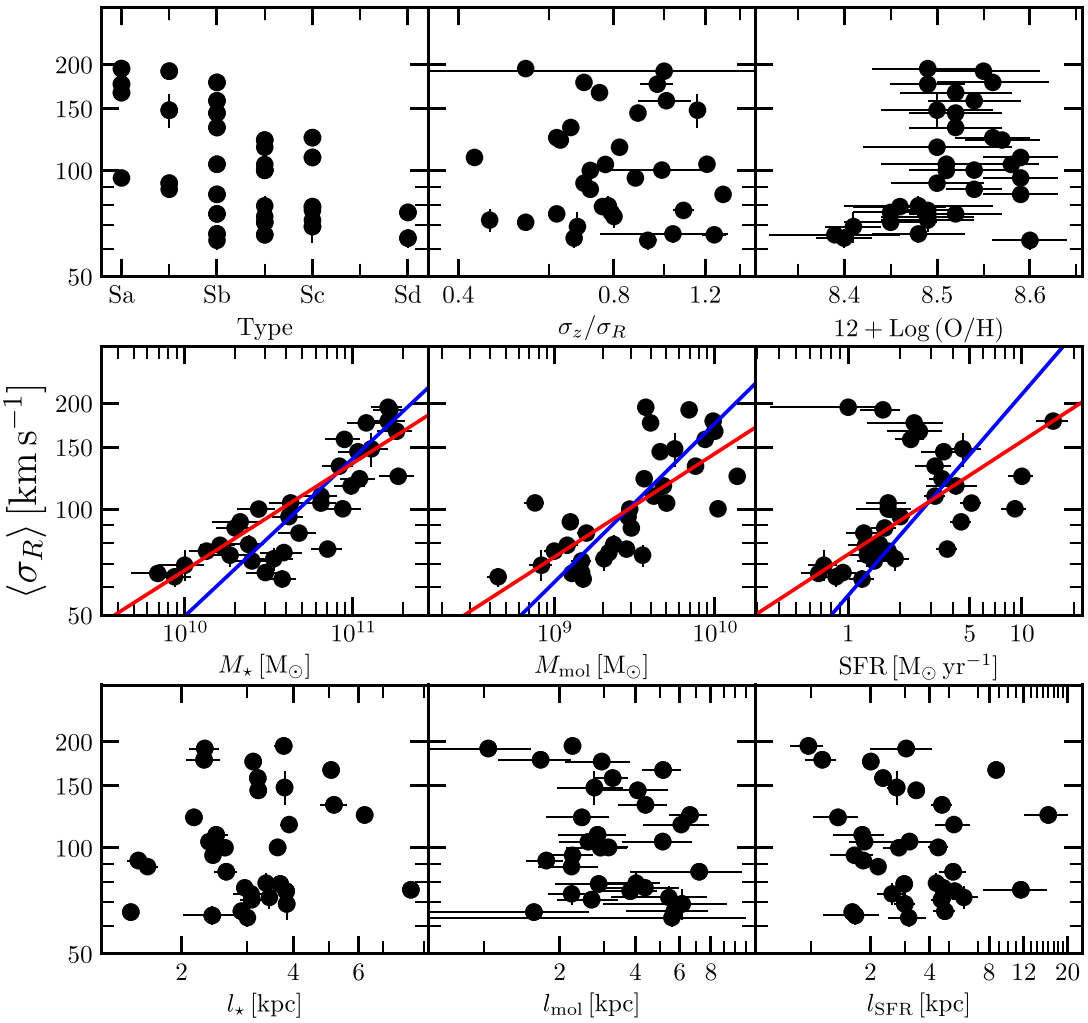

Figure 5. The radial average of the stellar radial velocity dispersion $\sigma_R(R)$ over 1 R_e, robustly estimated via the median, plotted as a function of Hubble type, B, metallicity, $M_\star$, $M_{\rm mol}$, SFR, $l_\star$, $l_{\rm mol}$, and $l_{\rm SFR}$. The red lines represent the best-fitting lines using a robust median-based fit method and the blue lines represent the best-fitting lines from ODR least-squares fitting.

Table 3. Correlation coefficients and best-fitting parameters for σ_R versus galaxy properties.

Property (1)	r_P (2)	p_P (3)	r_S (4)	p_S (5)	a (6)	b (7)	c (8)	d (9)	Δ (10)
Hubble stage (T)	−0.58	3.5×10^{-4}	−0.51	1.8×10^{-3}	–	–	–	–	–
σ_z/σ_R	0.00	1.0	0.00	9.9×10^{-1}	–	–	–	–	–
12+Log(O/H)	0.32	6.2×10^{-2}	0.44	1.0×10^{-2}	–	–	–	–	–
$M_\star$ (M$_\odot$)	0.82	2.2×10^{-9}	0.86	1.0×10^{-10}	0.30	−1.22	0.45 ± 0.05	−2.78 ± 0.51	0.10
$M_{\rm mol}$ (M$_\odot$)	0.69	5.6×10^{-6}	0.77	1.0×10^{-7}	0.29	−0.78	0.45 ± 0.06	−2.26 ± 0.62	0.12
SFR (M$_\odot$ yr^{-1})	0.42	1.3×10^{-2}	0.60	1.8×10^{-4}	0.32	1.87	0.57 ± 0.11	1.76 ± 0.05	0.18
$l_\star$ (kpc)	0.07	7.0×10^{-1}	0.10	5.6×10^{-1}	–	–	–	–	–
$l_{\rm mol}$ (kpc)	−0.28	1.1×10^{-1}	−0.20	2.7×10^{-1}	–	–	–	–	–
$l_{\rm SFR}$ (kpc)	−0.09	6.0×10^{-1}	−0.19	2.9×10^{-1}	–	–	–	–	–

Notes. Column 1: galaxy property; Column 2: Pearson's rank correlation coefficient; Column 3: p-value for Pearson's rank correlation; Column 4: Spearman's rank correlation coefficient; Column 5: p-value for Spearman's rank correlation; Columns 6,7: a and b parameters from the robust median-based fit $\log\langle\sigma_R\rangle = a\log X + b$, where X denotes galaxy property; Columns 8,9: c and d parameters from the ODR fit $\log\langle\sigma_R\rangle = c\log X + d$; Column 10: rms scatter of scaling relations.

contrary to the results of Westfall et al. (2014), who find that the gas component is more unstable than the stellar component. Unlike typical studies, they calculate $\Sigma_\star$ dynamically, resulting in lower $\Sigma_\star$ than those calculated via population synthesis, as seen when comparing their values to Martinsson et al. (2013), who they draw their sample from. However, their underestimation may be due to not taking into account the young thin component of the stellar disc and overestimating the scale height (Aniyan et al. 2016). Therefore,

Table 4. Observed versus model-based $\langle \sigma_R \rangle$.

Name	$\langle \sigma_R \rangle_{\rm obs}$ (km s^{-1})	$\langle \sigma_R \rangle_{\rm mod}$ (km s^{-1})	$\sqrt{GM_\star/l_\star}$ (km s^{-1})
(1)	(2)	(3)	(4)
IC 0480	74.0 ± 5.2	–	161.3 ± 16.9
IC 0944	166.4 ± 6.4	205.6 ± 5.4	393.4 ± 12.2
IC 2247	100.1 ± 2.6	–	212.7 ± 10.8
IC 2487	75.3 ± 1.8	120.6 ± 4.6	209.1 ± 5.5
NGC 2253	108.9 ± 1.9	137.3 ± 2.9	334.8 ± 24.5
NGC 2347	122.0 ± 2.5	146.9 ± 4.0	467.4 ± 13.7
NGC 2410	146.6 ± 3.2	181.1 ± 5.9	378.5 ± 15.7
NGC 2730	76.0 ± 4.0	55.4 ± 1.2	(123.6)[a]
NGC 4644	85.5 ± 1.9	119.2 ± 2.8	279.4 ± 19.3
NGC 4711	63.3 ± 3.7	–	233.2 ± 8.8
NGC 5056	77.0 ± 2.0	–	320.9 ± 9.1
NGC 5614	191.5 ± 3.2	137.9 ± 1.8	556.1 ± 50.8
NGC 5908	157.8 ± 1.7	143.3 ± 2.3	345.7 ± 8.2
NGC 5980	104.0 ± 2.3	–	342.4 ± 7.9
NGC 6060	116.4 ± 6.1	–	328.4 ± 17.9
NGC 6168	64.3 ± 4.0	77.1 ± 1.8	124.5 ± 20.6
NGC 6186	95.2 ± 2.0	–	271.7 ± 12.5
NGC 6314	194.8 ± 4.2	153.3 ± 4.1	430.3 ± 24.2
NGC 6478	124.0 ± 4.2	221.4 ± 5.3	358.7 ± 15.9
NGC 7738	177.9 ± 4.6	114.5 ± 3.0	550.9 ± 57.7
UGC 00809	69.3 ± 6.8	72.2 ± 2.1	105.9 ± 4.6
UGC 03253	104.2 ± 3.5	213.2 ± 9.3	275.4 ± 10.6
UGC 03539	65.7 ± 3.4	71.6 ± 3.0	142.8 ± 2.7
UGC 04029	79.4 ± 5.0	–	174.8 ± 8.4
UGC 04132	100.3 ± 3.1	194.9 ± 6.0	321.4 ± 14.6
UGC 05108	148.4 ± 16.0	173.5 ± 5.3	382.5 ± 10.8
UGC 05598	71.3 ± 2.9	87.5 ± 2.6	187.1 ± 12.9
UGC 09542	72.3 ± 5.2	–	205.6 ± 6.5
UGC 09873	79.0 ± 4.0	64.7 ± 2.6	137.5 ± 5.4
UGC 09892	66.1 ± 3.6	79.9 ± 2.3	211.7 ± 9.0
UGC 10123	88.4 ± 2.4	–	230.2 ± 15.8
UGC 10205	175.8 ± 2.2	143.4 ± 7.2	407.3 ± 12.3
UGC 10384	92.0 ± 3.1	99.3 ± 4.7	245.2 ± 16.4
UGC 10710	132.5 ± 5.9	100.1 ± 3.5	263.7 ± 21.6

Notes. Column 1: galaxy name; Column 2: median of observed σ_R; Column 3: median of model-based σ_R; Column 4: velocity scale.
[a]Model-based σ_R and velocity scale of NGC 2730 were calculated using $l_\star$ estimated from $R_{\rm e}$.

the uncertainties and assumptions of methods used to determine $\Sigma_\star$ and $M_\star$ should be further investigated to improve $M_\star$ estimates.

5.3 $\langle \sigma_R \rangle$–$M_\star$ relation

The $\langle \sigma_R \rangle$–$M_\star$ correlation we find is consistent with findings by Bottema (1992), who found a correlation between σ_R and the luminosity of the old disc. Unlike their luminosity correlation, we find a direct correlation with the stellar mass and this correlation has not been explicitly shown for nearby galaxies in terms of the total stellar mass until this study. An ∼0.5 power-law index would indicate that the L08 relation: $\langle \sigma_R \rangle \sim (\Sigma_\star\, l_\star)^{0.5}$ holds for properties averaged over an effective radius and scale length and is a consequence of discs in hydrostatic equilibrium and isothermal in the vertical direction. The result of the robust mean fit is a fitted lower power-law index of 0.3; however, this technique does not take into account uncertainties in σ_R and $M_\star$. Whereas the least-squares ODR fit, which takes into account uncertainties in both parameters, produces a fitted power-law index of 0.45 ± 0.05. The constant of proportionality is dependent on the flatness ratio and how close to

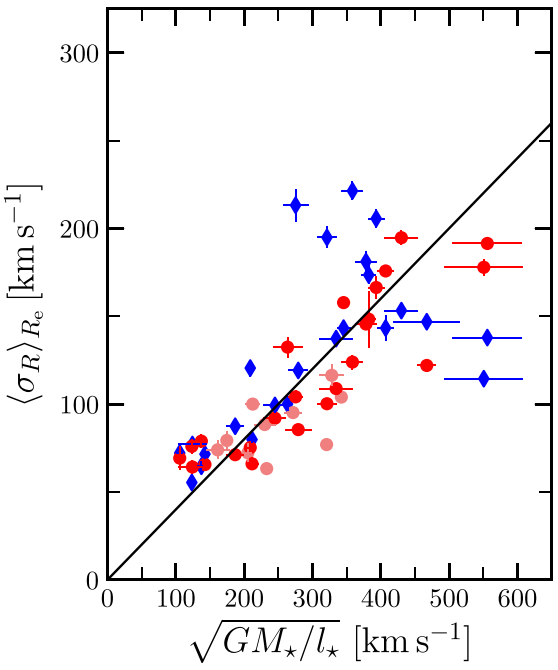

Figure 6. The radial averages of the stellar velocity dispersion $\sigma_R(R)$ (red circles) and model-based velocity dispersion $\sigma_{\rm mod}$ (R) (blue diamonds) over an effective radius $R_{\rm e}$, robustly estimated via the median, all plotted against the velocity scale: $\sqrt{GM_\star/l_\star}$. The dark red points show the subsample of galaxies for which we calculated model-based velocity dispersions. A $\langle \sigma_R \rangle$=0.4$\sqrt{GM_\star/l_\star}$ relation is shown by the black line.

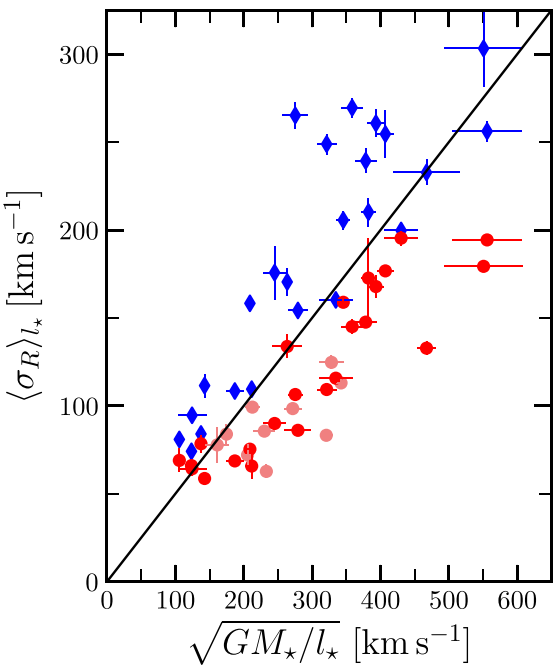

Figure 7. The radial averages of the stellar velocity dispersion $\sigma_R(R)$ (red circles) and model-based velocity dispersion $\sigma_{\rm mod}$ (R) (blue diamonds) over the stellar scale length $l_\star$, robustly estimated via the median, all plotted against the velocity scale: $\sqrt{GM_\star/l_\star}$. The dark red points show the subsample of galaxies for which we calculated model-based velocity dispersions. A $\langle \sigma_R \rangle$=0.5$\sqrt{GM_\star/l_\star}$ relation is shown by the black line.

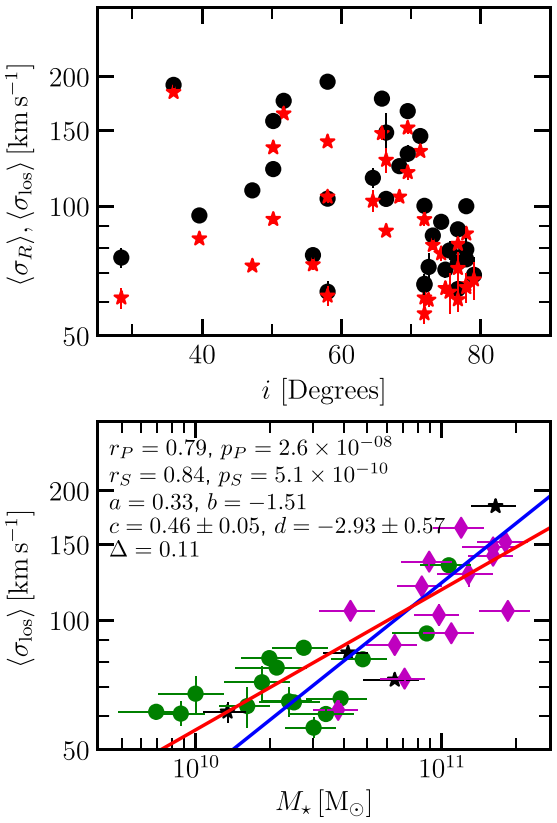

Figure 8. Top: Plot comparing the radial averages of the radial (black circles) and line-of-sight (red stars) stellar velocity dispersions, averaged over 1 R_e, robustly estimated via the median: $\langle\sigma_R\rangle$ and $\langle\sigma_{\rm los}\rangle$, respectively, as a function of inclination. Bottom: $\langle\sigma_{\rm los}\rangle$ as a function of $M_\star$. Galaxies with $i < 50^\circ$ are shown as black stars, those with $50^\circ < i < 70^\circ$ as magenta diamonds, and galaxies with $i > 70^\circ$ are shown as green circles. The red line represents the best-fitting line using a robust median-based fit method and the blue line represents the best-fitting line from ODR least-squares fitting.

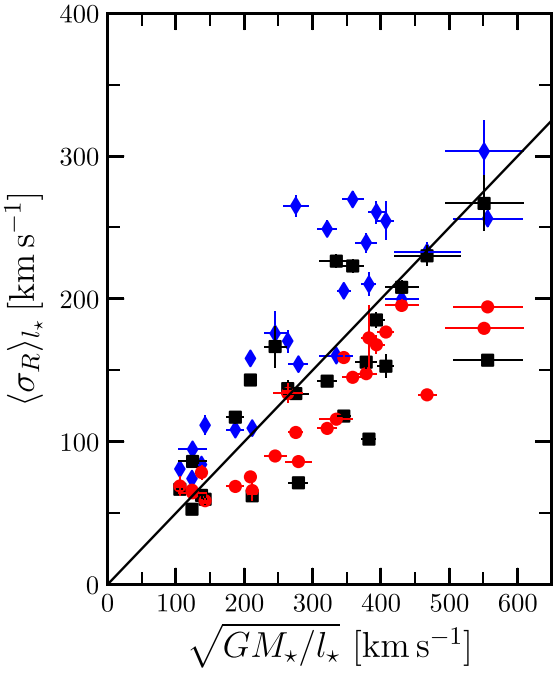

Figure 9. The radial averages of the stellar velocity dispersion $\sigma_R(R)$ (red circles) and model-based velocity dispersions $\sigma_{\rm mod}$ (R) all averaged over the stellar scale length $l_\star$, robustly estimated via the median, and all plotted against the velocity scale: $\sqrt{GM_\star/l_\star}$. $\sigma_{\rm mod}$ (R) values calculated using $B = 0.6$ and a flattening ratio of 7.3 are shown as blue diamonds and $\sigma_{\rm mod}$ (R) calculated using K17 B and Bershady et al. (2010) flattening ratios are shown as black squares. We only show galaxies for which we calculated model-based velocity dispersions. A $\langle\sigma_R\rangle$=0.5$\sqrt{GM_\star/l_\star}$ relation is shown by the black line.

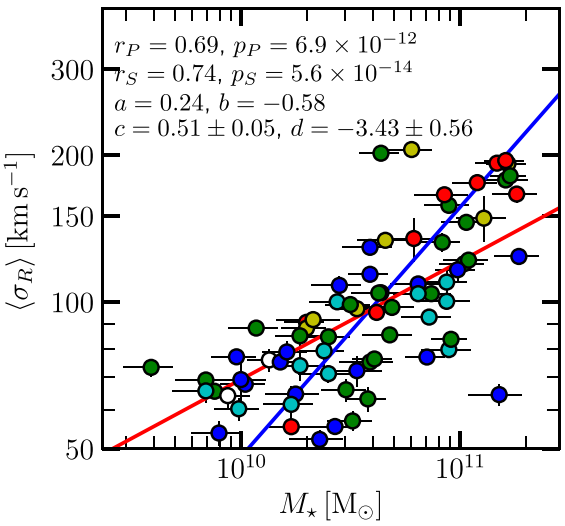

Figure 10. The radial average of the stellar radial velocity dispersion $\sigma_R(R)$ over 1 R_e, robustly estimated via the median, plotted as a function of $M_\star$ for the larger sample of galaxies with $\sigma_{\rm los}$, circular-speed curve and stellar mass data. The red line represents the best-fitting line from a robust median-based fit method and the blue line represents the best-fitting line from least-squares fitting. The galaxies are coded according to Hubble type: Sa galaxies are shown in red, Sab in yellow, Sb in green, Sbc in cyan, Sc in blue, and Sd galaxies are shown in white.

exponential the discs are, both of which require further analysis and larger samples to better constrain.

Now we test the robustness of the $\langle\sigma_R\rangle$–$M_\star$ relationship against sample size by using a larger sample of spiral galaxies (i.e. Hubble types ranging from Sa to Sd) that have both σ_R, circular-speed curves and $M_\star$ measurements from F-B17, K17, and B17. This larger sample consists of 74 galaxies. We plot $\langle\sigma_R\rangle$ versus $M_\star$ for the sample in Fig. 10 and find that the $\langle\sigma_R\rangle$–$M_\star$ correlation still holds. The significance of the correlation is higher than for the small sample: $p_{\rm P} = 6.9 \times 10^{-12}$ and $p_{\rm S} = 5.6 \times 10^{-14}$ and the strength of the correlation is $r_{\rm P} = 0.69$ and $r_{\rm S} = 0.74$. The best-fitting parameters are similar to the results for the small sample and the slope of the relationship is closer to 0.5 when using ODR fits: $c = 0.51 \pm 0.05$ and $d = -3.40 \pm 0.56$. The rms scatter of the relation is 0.15. The power-law index from the robust median fit is 0.24. The correlation coefficients and their null hypothesis tests confirm the robustness of the correlation between $\langle\sigma_R\rangle$ and $M_\star$ regardless of the sample size.

To test whether the inconsistencies between the ODR and robust median fits are due to uncertainties in the data, we perform least-squares fit to the data from the smaller sample, assuming that both parameters have zero uncertainties. The power-law index from this fit is 0.39 ± 0.05. For the larger sample, the least-

Table 5. Correlation coefficients and best-fitting parameters for $\delta\log\langle\sigma_R\rangle$ versus galaxy properties.

Property (1)	r_S (2)	p_S (3)	c (4)	d (5)
$M_\star$ ($M_\odot$)	−0.52	0.002	−0.49 ± 0.15	5.21 ± 1.62
M_{mol} ($M_\odot$)	−0.39	0.022	–	–
SFR ($M_\odot\,yr^{-1}$)	−0.40	0.018	−0.71 ± 0.24	0.24 ± 0.10

Notes. Column 1: galaxy property; Column 2: Spearman's rank correlation coefficient; Column 3: p-value for Spearman's rank correlation; Columns 4,5: c and d parameters from the ODR fit $\delta\log\langle\sigma_R\rangle = c\log X + d$.

squares fit with zero uncertainties has a power-law index fit of 0.34 ± 0.03. Therefore, not taking into account the uncertainties of both $M_\star$ and $\langle\sigma_R\rangle$ results in underestimation of the power-law index. When uncertainties are taken into account, the power-law index of relationship between $\langle\sigma_R\rangle$ and $M_\star$ is close to 0.5.

To fully characterize the $\langle\sigma_R\rangle$–$M_\star$ correlation, we have also analysed its scatter:

$$\delta\log\langle\sigma_R\rangle = \log\langle\sigma_R\rangle - \log\langle\sigma_R\rangle_{fit}, \quad (6)$$

where $\log\langle\sigma_R\rangle_{fit} = 0.45\log M_\star - 2.78$ is the ODR best-fitting relation (see Table 3). The statistical measurements given in Table 5 show that $\delta\log\langle\sigma_R\rangle$ has a residual anticorrelation with $M_\star$, but this is weaker and less significant than the primary $\langle\sigma_R\rangle$–$M_\star$ correlation. This is then a second-order effect, which has no significant impact on our results.

5.4 $\langle\sigma_R\rangle$ relation with other parameters

The galaxy main sequence (e.g. Daddi et al. 2007; Elbaz et al. 2007; Noeske et al. 2007; Catalán-Torrecilla et al. 2017) shows the correlation between $M_\star$ and SFR. Hubble type is inversely proportional to stellar mass and metallicity is correlated with stellar mass via the mass–metallicity relation (e.g. Lequeux et al. 1979; Tremonti et al. 2004; Sánchez et al. 2017). Therefore, the correlation and anticorrelation between SFR, Hubble type, and metallicity with $\langle\sigma_R\rangle$ can be put in terms of the stellar mass. Gerssen et al. (2012) found a correlation between σ_R and molecular gas surface density, therefore the $\langle\sigma_R\rangle$–M_{mol} correlation can be thought of as a reflection of that, and it hints that GMCs may play a role in disc heating. The non-correlation between σ_z/σ_R and $\langle\sigma_R\rangle$ is expected (e.g. Gerssen et al. 2012) and hints that there is a component of disc heating that only affects σ_R. The $\langle\sigma_R\rangle$ versus $M_\star$, M_{mol}, and SFR relations have similar power-law indices, which is consistent with observations that show that the stellar and molecular discs approximately track each other (e.g. B17).

We also study the scatter of the M_{mol} and SFR relations in a similar manner to $M_\star$ and the correlations and results of the fits are shown in Table 5. It should be noted that the applicable $\langle\sigma_R\rangle_{fit}$ was used to calculate appropriate $\delta\log\langle\sigma_R\rangle$ values for each case, according to the fit results shown in Table 3. The results show that the anticorrelations between M_{mol} and SFR and their $\delta\log\langle\sigma_R\rangle$ are weaker and less significant than for $M_\star$: $r_S = -0.39$, $p_S = 0.022$ for M_{mol} and $r_S = -0.40$ and $p_S = 0.018$ for SFR. The best-fitting relation for $\delta\log\langle\sigma_R\rangle$ versus log SFR has a slope of −0.71. We could not achieve a good fit to the data for $\delta\log\langle\sigma_R\rangle$ versus $\log M_{mol}$ using the ODR method. In both the cases, the correlations are also much weaker than the fit relations shown in Table 3.

We next explore the relationship between $\langle\sigma_R\rangle$ and molecular fraction and specific star formation. We remove the effects of the $\langle\sigma_R\rangle$–$M_\star$ correlation and plot $\langle\sigma_R\rangle M_\star^{-0.45}$ versus M_{mol}, SFR, and $M_\star$ for the 34 galaxy sample in Fig. 11. This allows us to study the aforementioned relationships. The best-fitting relations and correlation coefficients from these plots are shown in Table 6. Fig. 11 shows that there is little correlation between $\langle\sigma_R\rangle M_\star^{-0.45}$ and $M_\star$ for galaxies with $M_\star > 2\times10^{10}M_\odot$ and an anticorrelation between them at smaller $M_\star$. The anticorrelation between $M_\star$ and $\langle\sigma_R\rangle M_\star^{-0.45}$ is weak ($r_S = -0.52$, $p_S = 1.7\times10^{-3}$) and has a best-fitting power-law index of −0.12 ± 0.04. M_{mol} and SFR have weaker and less significant anticorrelations with $\langle\sigma_R\rangle M_\star^{-0.45}$ and their best-fitting power-law indices range between −0.09 ± 0.04 and −0.14 ± 0.05, respectively. Their fitted power-law indices are consistent with the $\langle\sigma_R\rangle M_\star^{-0.45}$ versus $M_\star$ relation's fitted power-

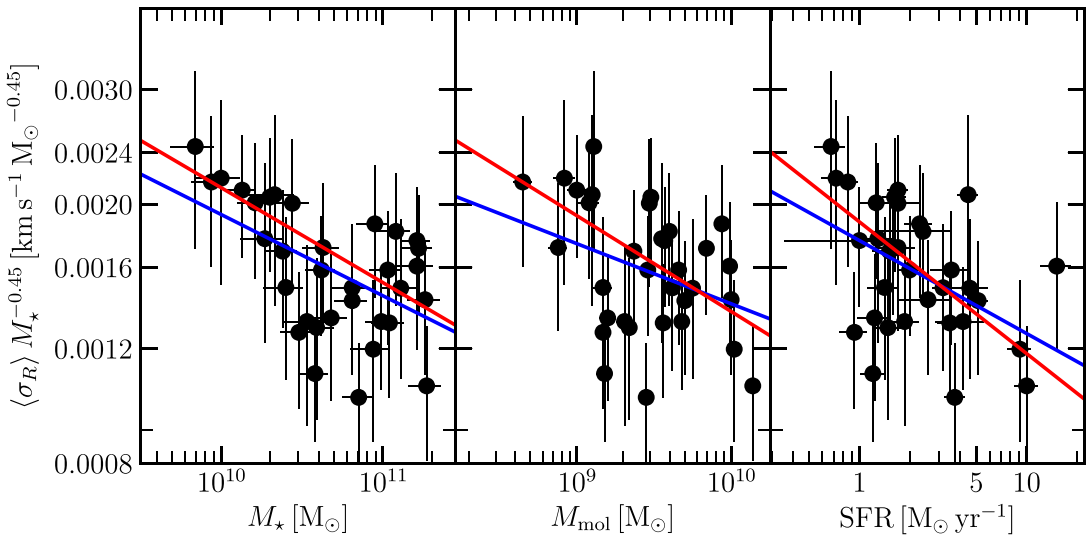

Figure 11. The radial average of the stellar radial velocity dispersion $\sigma_R(R)$ over 1 R_e, robustly estimated via the median, divided by $M_\star^{0.45}$ and plotted as a function of $M_\star$, M_{mol}, and SFR. This allows us to study the relationship between the radial average of the stellar radial velocity dispersion and the molecular fraction and specific star formation. The red lines represent the best-fitting lines using a robust median-based fit method and the blue lines represent the best-fitting lines from ODR least-squares fitting.

Table 6. Correlation coefficients and best-fitting parameters for $\sigma_R/M_\star^{-0.45}$ versus galaxy properties.

Property (1)	r_P (2)	p_P (3)	r_S (4)	p_S (5)	a (6)	b (7)	c (8)	d (9)	Δ (10)
$M_\star$ ($M_\odot$)	−0.61	1.5×10^{-4}	−0.52	1.7×10^{-3}	−0.15	−1.22	−0.12 ± 0.04	−1.47 ± 0.40	0.08
M_{mol} ($M_\odot$)	−0.44	9.3×10^{-3}	−0.39	2.2×10^{-2}	−0.15	−1.39	−0.09 ± 0.04	−1.93 ± 0.42	0.09
SFR ($M_\odot$ yr^{-1})	−0.47	5.5×10^{-3}	−0.40	1.8×10^{-2}	−0.20	−2.73	−0.14 ± 0.05	−2.76 ± 0.02	0.09

Notes. Column 1: galaxy property; Column 2: Pearson's rank correlation coefficient; Column 3: p-value for Pearson's rank correlation; Column 4: Spearman's rank correlation coefficient; Column 5: p-value for Spearman's rank correlation; Columns 6,7: a and b parameters from the robust median-based fit $\log\langle\sigma_R\rangle = a\log X + b$, where X denotes galaxy property; Columns 8,9: c and d parameters from the ODR fit $\log\langle\sigma_R\rangle = c\log X + d$; Column 10: rms scatter of scaling relations.

law index. It should be noted that the quantities in the leftmost plot in Fig. 11 are directly correlated, and as mentioned before there are also correlations between the quantities in the other plots, therefore care should be taken when attempting to identify correlations from these plots. Existing SFR and M_{mol} correlations with $M_\star$, the consistency between power-law indices, and the low significance of the correlations (e.g.Table 6) suggest that the SFR and M_{mol} relationships are dominated by the stronger and more significant $M_\star$ anticorrelation that exists at low $M_\star$. However, we require more high-quality data to investigate this further and determine whether there are any correlations between $\langle\sigma_R\rangle$ and either the molecular fraction or specific star formation.

6 CONCLUSIONS

In this study, we have used observed line-of-sight σ_{los} and fitted dispersion anisotropy parameters to determine σ_R for 34 galaxies from the CALIFA survey. These galaxies cover a wide range of properties such as Hubble types ranging from Sa to Sd. We compare σ_R values to model-based σ_R, study how they change with radius, and study how they relate to galaxy properties. Our major conclusions are as follows:

(i) Model-based dispersions overestimate σ_R at small radii. The difference can be greater than 50 km s^{-1} within a stellar scale length. Therefore, model-based dispersions do not accurately model σ_R and the use of high-quality stellar line-of-sight velocity dispersions will result in more accurate stability parameters, asymmetric drift corrections, and better constraints on disc heating processes.

(ii) The radial average of σ_R over the effective radius is correlated with $M_\star$, M_{mol}, and SFR, and it is weakly correlated with metallicity and weakly anticorrelated with Hubble type. The $\langle\sigma_R\rangle$ versus SFR, metallicity, and Hubble type relations can be thought of in terms of the $\langle\sigma_R\rangle$–$M_\star$ relation, which has the strongest and most significant correlation. And the best-fitting line to the relation is: $\log\langle\sigma_R\rangle = 0.45\log M_\star - 2.78$, with an rms scatter of 0.10 dex compared to 0.12 and 0.18 dex for M_{mol} and SFR using similar samples. For a larger sample of 74 galaxies, the best-fitting line to the $\langle\sigma_R\rangle$–$M_\star$ relation is: $\log\langle\sigma_R\rangle = 0.51\log M_\star - 3.43$, with an rms scatter of 0.15 dex. This $\langle\sigma_R\rangle \propto M_\star{}^{0.5}$ relation is important and can be used in conjunction with other scaling relations to measure disc stability and to show that nearby disc galaxies self-regulate to a quasi-universal disc stability level (Romeo & Mogotsi 2018).

(iii) The results found in this paper confirm, with a large sample of nearby star-forming spirals, the findings of Romeo & Mogotsi (2017): using observed, rather than model-based, stellar radial velocity dispersions leads to less stable inner galaxy discs and to disc instabilities driven even more by the self-gravity of stars. This shows, once again, how important it is to rely on high-quality measurements of the stellar line-of-sight velocity dispersion, such as those provided by the CALIFA, SAMI, and MaNGA surveys and those promised by second-generation IFU surveys using the Multi Unit Spectroscopic Explorer (MUSE).

ACKNOWLEDGEMENTS

KMG acknowledges support from the National Research Foundation of South Africa. We wish to thank the referee for useful comments and suggestions that helped to improve this paper. This study uses data provided by the Calar Alto Legacy Integral Field Area (CALIFA) survey (http://califa.caha.es/). Based on observations collected at the Centro Astronómico Hispano Alemán (CAHA) at Calar Alto, operated jointly by the Max-Planck-Institut für Astronomie and the Instituto de Astrofísica de Andalucía (CSIC).

REFERENCES

Allen J. T. et al., 2015, MNRAS, 446, 1567
Aniyan S., Freeman K. C., Gerhard O. E., Arnaboldi M., Flynn C., 2016, MNRAS, 456, 1484
Aniyan S. et al., 2018, MNRAS, 476, 1909
Bershady M. A., Verheijen M. A. W., Westfall K. B., Andersen D. R., Swaters R. A., Martinsson T., 2010, ApJ, 716, 234
Binney J., Merrifield M., 1998, Galactic Astronomy. Princeton Univ. Press, Princeton, NJ
Binney J., Tremaine S., 2008, Galactic Dynamics. Princeton Univ. Press, Princeton, NJ
Binney J., Dehnen W., Bertelli G., 2000, MNRAS, 318, 658
Bolatto A. D. et al., 2017, ApJ, 846, 159
Bottema R., 1992, A&A, 257, 69
Bundy K. et al., 2015, ApJ, 798, 7
Cappellari M., 2008, MNRAS, 390, 71
Cappellari M., Copin Y., 2003, MNRAS, 342, 345
Catalán-Torrecilla C. et al., 2017, ApJ, 848, 87
Chemin L., 2018, A&A, 618, A121
Daddi E. et al., 2007, ApJ, 670, 156
Dehnen W., 1998, AJ, 115, 2384
Dehnen W., Binney J. J., 1998, MNRAS, 298, 387
Elbaz D. et al., 2007, A&A, 468, 33
Falcón-Barroso J. et al., 2017, A&A, 597, A48
Feigelson E. D., Babu G. J., 2012, Modern Statistical Methods for Astronomy with R Applications. Cambridge Univ. Press, Cambridge
García-Benito R. et al., 2015, A&A, 576, A135
Gerssen J., Shapiro Griffin K., 2012, MNRAS, 423, 2726
Gerssen J., Kuijken K., Merrifield M. R., 1997, MNRAS, 288, 618
Gerssen J., Kuijken K., Merrifield M. R., 2000, MNRAS, 317, 545
González Delgado R. M. et al., 2014, A&A, 562, A47
Hessman F. V., 2017, MNRAS, 469, 1147
Huber P. J., Ronchetti E. M., 2009, Robust Statistics. Wiley, Hoboken, NJ
Husemann B. et al., 2013, A&A, 549, A87
Jenkins A., Binney J., 1990, MNRAS, 245, 305
Kalinova V., van de Ven G., Lyubenova M., Falcón-Barroso J., Colombo D., Rosolowsky E., 2017a, MNRAS, 464, 1903

Kalinova V. et al., 2017b, MNRAS, 469, 2539
Kregel M., van der Kruit P. C., 2005, MNRAS, 358, 481
Kregel M., van der Kruit P. C., de Grijs R., 2002, MNRAS, 334, 646
Lequeux J., Peimbert M., Rayo J. F., Serrano A., Torres-Peimbert S., 1979, A&A, 80, 155
Leroy A. K., Walter F., Brinks E., Bigiel F., de Blok W. J. G., Madore B., Thornley M. D., 2008, AJ, 136, 2782
Marchuk A. A., Sotnikova N. Y., 2017, MNRAS, 465, 4956
Martinsson T. P. K., Verheijen M. A. W., Westfall K. B., Bershady M. A., Andersen D. R., Swaters R. A., 2013, A&A, 557, A131
Müller J. W., 2000, J. Res. Natl. Inst. Stand. Technol., 105, 551
Noeske K. G. et al., 2007, ApJ, 660, L43
Pinna F., Falcón-Barroso J., Martig M., Martínez-Valpuesta I., Méndez-Abreu J., van de Ven G., Leaman R., Lyubenova M., 2018, MNRAS, 475, 2697
Press W. H., Teukolsky S. A., Vetterling W. T., Flannery B. P., 1992, Numerical Recipes in Fortran: The Art of Scientific Computing. Cambridge Univ. Press, Cambridge
Rafikov R. R., 2001, MNRAS, 323, 445
Rodionov S. A., Sotnikova N. Y., 2013, MNRAS, 434, 2373
Romeo A. B., Falstad N., 2013, MNRAS, 433, 1389
Romeo A. B., Fathi K., 2015, MNRAS, 451, 3107
Romeo A. B., Fathi K., 2016, MNRAS, 460, 2360
Romeo A. B., Mogotsi K. M., 2017, MNRAS, 469, 286
Romeo A. B., Mogotsi K. M., 2018, MNRAS, 480, L23
Romeo A. B., Horellou C., Bergh J., 2004, MNRAS, 354, 1208
Rousseeuw P. J., 1991, J. Chemometr., 5, 1
Sánchez S. F. et al., 2012, A&A, 538, A8
Sánchez S. F. et al., 2016, Rev. Mex. Astron. Astrofis., 52, 171
Sánchez S. F. et al., 2017, MNRAS, 469, 2121
Schwarzschild K., 1907, Akad. Wiss. Göttingen Nachr., 614
Shapiro K. L., Gerssen J., van der Marel R. P., 2003, AJ, 126, 2707
Spitzer L., Jr., Schwarzschild M., 1951, ApJ, 114, 385
Tian H.-J. et al., 2015, ApJ, 809, 145
Toomre A., 1964, ApJ, 139, 1217
Tremonti C. A. et al., 2004, ApJ, 613, 898
van der Kruit P. C., 1988, A&A, 192, 117
van der Kruit P. C., Searle L., 1981, A&A, 95, 105
Walcher C. L. et al., 2014, A&A, 569, A1
Westfall K. B., Andersen D. R., Bershady M. A., Martinsson T. P. K., Swaters R. A., Verheijen M. A. W., 2014, ApJ, 785, 43
Wielen R., 1977, A&A, 60, 263

This paper has been typeset from a TEX/LATEX file prepared by the author.